An Adaptive Discontinuous Galerkin Method on Unstructured Meshes for the Simulation of Hurricane Storm Surge

N. Beisiegel*[1,2], S. Vater[3], J. Behrens[4,6], and F. Dias[1,2,5]

[1]Earth Institute, University College Dublin, Dublin, Ireland
[2]School of Mathematics & Statistics, University College Dublin, Dublin, Ireland
[3]Institute of Mathematics, Freie Universität Berlin, Berlin, Germany
[4]Department of Mathematics, Universität Hamburg, Hamburg, Germany
[5]CMLA, École Normale Supérieure, Paris-Saclay, France
[6]Center for Earth System Research and Sustainability, Universität Hamburg, Hamburg, Germany

Numerical simulations based on solving the 2D shallow water equations using a Discontinuous Galerkin (DG) discretisation have evolved to be a viable tool for many geophysical applications. In the context of flood modelling, however, they have not yet been methodologically studied to a large extent. On geographic scale, hurricane storm surge can be interpreted as a localised phenomenon making it ideally suited for adaptive mesh refinement (AMR). Past studies employing dynamic AMR have exclusively focused on nested meshes. For that reason we have developed a DG storm surge model on a triangular and dynamically adaptive mesh. In order to increase computational efficiency, the refinement is driven by physics-based refinement indicators capturing major model sensitivities. Using idealised numerical test cases, we demonstrate the model's ability to correctly represent all source terms and reproduce known variability of coastal flooding with respect to hurricane characteristics such as size and approach speed. Finally, the unstructured mesh significantly reduces computing time with no effect on storm waves measured at discrete wave gauges just off the coast which shows the model's capability for use as a robust simulation tool for real-time predictions.

Keywords: Storm Surges, Discontinuous Galerkin, Wind Stress, Wind Drag, Adaptive Mesh Refinement, Shallow Water Equations

1 Introduction

Extreme storms and floods are among the most devastating natural disasters worldwide faced by inhabitants of coastal areas and those whose livelihood depends on marine resources alike (see e.g. [24]). Their accurate simulation and prediction is vital for hazard assessment and the implementation of mitigation strategies such as the opening and closing of flood barriers in order to protect local populations and property. Due to the time critical nature of forecasts, current operational simulation environments that form the basis of flood forecasts are chosen for their robustness and optimised run time. However, this efficiency comes at the cost of having to use reduced hydrodynamical model approximations for the underlying processes and simplified parameterisations for physical forcing terms. This means that operational models often do not model the full physics [35]. Instead, such simple inundation models simply raise water levels to a given constant elevation. Linear approaches like this are computationally inexpensive and work well for generalised scenarios and at broad geographic scale, but as we become more specific and local in the attempted projections, the complexities multiply, and non-linearities become more significant in the behaviour of the modelled physical processes. Therefore, we cannot use linear mathematical approaches to precisely model these situations. Non-linear models, on the other hand, can be costly and the high-order information they contain might require advanced filtering to guarantee numerical robustness and efficiency. These more accurate models, however, are of critical importance. As was shown in [3] the accuracy of projections for future events, in particular with respect to our changing climate, depends on the accurate modelling of small scale physical dynamics at large scale.

*nicole.beisiegel@ucd.ie

In this study we focus on Discontinuous Galerkin (DG) methods to solve the 2D non-linear shallow water equations. These depth integrated equations are computationally less demanding than more accurate 3D Navier-Stokes equations and have been shown to yield good results for coastal applications. DG methods have recently gained a lot of attention for geophysical applications because of their local mass conservation, and geometric flexibility. Moreover, numerical computations are performed locally since elements only communicate over element interfaces (edges) through the computation of numerical fluxes. This is a particular advantage for current state-of-the-art computational architectures and although beyond the scope of this study, we remark that the local nature of this discretisation makes it ideal for parallelisation as shown for example in [1].

Current operational flood models do not employ DG discretisations; they are based on other numerical techniques. A common choice is continuous finite elements [28], because they work well with non-uniform meshes. However, they only yield global mass conservation and parallelisation is more difficult because large linear systems often need to be inverted. The majority of computer models used in practice rely on finite difference discretisations. Those have the advantage of discretisations for parameterisations of source terms such as bottom friction being existent and well established. We remark, though, that in theory the implementation of parameterisations in a DG framework would be easy as it offers the opportunity to control in cell values as opposed to point values only and it does not formally require differentiability of the source term. Moreover, complex coastlines cannot easily be implemented well in a finite difference framework, since this discretisation is usually based on Cartesian meshes.

A higher computational efficiency of mesh-based numerical methods such as DG methods can be achieved by using non-uniform meshes [29] or dynamical adaptive mesh refinement as in [7], leading to an improved performance on current computing architectures. DG methods have been successfully employed in combination with a non-uniform but static mesh to hindcast the coastal flooding caused by hurricane Ike [11]. Ideally, and to save computational time, the use of dynamically adaptive non-uniform meshes would be preferable. These meshes are usually driven by either heuristic (or physics-based) refinement indicators, or error estimators that are based on model sensitivities which in turn can be derived from solving adjoint equations, as in [12] for a finite element framework. Solving adjoint equations, however, can be computationally expensive as it requires the solution of a different set of equations backwards in time with coefficients that result from the forward solution of the system. This increases memory requirements significantly. Additionally, [4] show that the discontinuous nature of DG methods poses systematic difficulties on deriving appropriate adjoint equations. The additional flexibility of a dynamically adaptive mesh would decrease the dependence of a high level of mesh optimisation that is particular for the geographic region of interest. An approach using Finite Volumes on a quadrilateral nested mesh has been used in one previous study [26], but the full potential of dynamically adaptive mesh refinement using physics-based refinement indicators for fully unstructured meshes is yet to be explored. Hence this study aims at investigating DG methods for flood applications on a dynamically adaptive triangular mesh.

The accurate modelling of inundation using the shallow water equations is mathematically challenging as the interface between water and land becomes a moving boundary, and the theoretical validity of the underlying equations breaks down in near-dry regions. Recently developed numerical methods show improved robustness due to improved limiting and filtering techniques [36, 37]. We will adopt the novel limiting strategy presented in [37] which features a velocity-based reconstruction of the momentum and allows us to compute meaningful velocities even close to the wet/dry interface.

The major driving force of storm surges are extreme winds and pressure gradients. This study considers hurricane storm surges in section 3.4 and employs the cyclonic wind model by [16] to compute continuous wind fields as well as corresponding atmospheric pressures. Finally, we implement all source terms that are relevant for coastal flooding and storm waves and show that in combination with the dynamically adaptive mesh refinement as proposed in [7] we built a new model that is suitable for coastal storm surge modelling.

In summary, in this study we combine a DG model with a dynamically adaptive unstructured mesh that is driven by physics-based refinement indicators. We show that recently developed advanced limiting strategy to treat wetting and drying as well as the discrete implementation of all relevant source terms lead to robust and accurate results on this mesh.

This paper is organised as follows. Section 2 outlines the numerical model and summarises the implementation of all relevant source terms. Section 3 presents a number of numerical test cases ranging from analytical to idealised yet realistic scenarios that showcase the model's inundation stability and conservation properties, the robustness of the wind forcing as well as its suitability for idealised storm surge modelling on a dynamically adaptive mesh. The final section 4 gives an outlook for future work

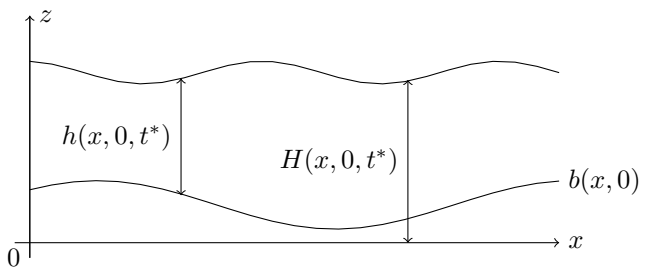

Figure 1: 2D Shallow Water Equations: Sketch of variables h, H and b, projection onto $y = 0$ at time $t = t^*$. Here, z is an upward pointing vertical coordinate.

and discusses implications, shortfalls and limitations of the study.

2 A Discontinuous Galerkin Discretisation of the Full 2D Non-Linear Shallow Water Equations

The system of equations of interest for this study are depth-integrated shallow water equations in two dimensions which can be written in flux form

$$\frac{\partial \mathbf{U}}{\partial t} + \nabla \cdot \mathbf{F}(\mathbf{U}) = S(\mathbf{U}) \quad \text{in} \quad \Omega \times T, \tag{1}$$

where the prognostic variables are $\mathbf{U} = (h, h\mathbf{u})^\top$: the water depth h and the 2D momentum $h\mathbf{u}$ defined on $\Omega \times T$, with $\Omega \subset \mathbb{R}^2$ and T a finite time interval. Spatial coordinates are denoted as $\mathbf{x} = (x, y)^\top \in \Omega$. The partial temporal derivative is denoted by $\frac{\partial \mathbf{U}}{\partial t}$ and $\nabla \cdot := \left(\frac{\partial}{\partial x}, \frac{\partial}{\partial y}\right) \cdot$ is the 2D divergence operator. The flux $\mathbf{F}$ and source term S are defined as

$$\mathbf{F}(\mathbf{U}) = \begin{bmatrix} h\mathbf{u} \\ h\mathbf{u} \otimes \mathbf{u} + \frac{g}{2} h^2 \mathbf{I}_2 \end{bmatrix}, \quad S(\mathbf{U}) = - \begin{bmatrix} 0 \\ gh\nabla b + \boldsymbol{\tau}_C - \rho^{-1} \left(\boldsymbol{\tau}_W + h\nabla p_A + \boldsymbol{\tau}_B \right) \end{bmatrix} \tag{2}$$

where $g = 9.81[ms^{-2}]$ is the acceleration due to gravity and $\mathbf{I}_2$ is the 2×2 identity matrix. We denote the temporally constant bathymetry by $b = b(\mathbf{x})$ and introduce the notation $H(\mathbf{x}, t) = h(\mathbf{x}, t) + b(\mathbf{x})$ for the total height (see also Figure 1). In addition to the influence of bathymetry, the source term S comprises a Coriolis forcing $\boldsymbol{\tau}_C$, a vector-valued wind stress $\boldsymbol{\tau}_W$, the water density ρ, the atmospheric pressure p_A, and a bottom friction $\boldsymbol{\tau}_B$ which are described in more detail in subsection 2.1. Throughout this paper vector valued quantities are indicated by a bold print while all other quantities are assumed to be scalar.

We discretise equation (1) using a Discontinuous Galerkin approach comprised of (a) decomposing the domain $\Omega = \sum_i \Omega_i$ into triangles, (b) approximating $\mathbf{U} = \sum_k \mathbf{U}_k(t)\phi_k(x)$ by linear Lagrange polynomials locally in each triangle and (c) integrating locally in space against test functions. Our test functions are linear Lagrange polynomials, so that the resulting semi-discrete system reads

$$\int_{\Omega_i} \mathbf{U}_t \phi_j \mathrm{d}\mathbf{x} + \int_{\Omega_i} \nabla \cdot \mathbf{F}(\mathbf{U}) \ \phi_j \mathrm{d}\mathbf{x} + \int_{\partial\Omega_i} (\mathbf{F}^*(\mathbf{U}) - \mathbf{F}(\mathbf{U})) \cdot \mathbf{n} \ \phi_j \mathrm{dS} = \int_{\Omega_i} S(\mathbf{U}) \phi_j \mathrm{d}\mathbf{x}. \tag{3}$$

In equation (3), $\mathbf{F}^*$ is a numerical Rusanov flux at the cell interfaces [34]. Note, that we integrated the flux integral by parts twice to obtain the often called strong form [15]. This form has desirable properties with respect to well-balancing as shown in [9] and elaborated in more detail in subsection 2.1.3. We solve the integrals in equation (3) with an interpolatory Gauss quadrature with corresponding Gauss-Legendre points.

This allows to extract the time derivative and after re-organisation, write the system (3) as a system of equations in t of the form

$$\frac{d\mathbf{U}_k}{dt} = \mathbf{H}(\mathbf{U}_k) \tag{4}$$

where $\mathbf{H}$ denotes the discretised flux and source terms. This system (4) can be solved using a SSP multi-stage Runge Kutta method provided suitable boundary conditions. If not indicated otherwise, we used Heun's method (RK22) for this study.

The slope limiter we are using is velocity-based and non-destructive with respect to well-balancing and non-negativity preservation. More detail can be found in [37] where it was successfully applied to tsunami benchmark test cases and to model flood scenarios. In the present study we show that it can be used as well for accurate shore line modelling and the reduction of spurious oscillations on unstructured meshes even when a variety of source terms are involved.

2.1 Implementation of Source Terms

Coastal flooding is a problem involving the interplay between many source terms. The source terms directly impact the momentum and, thus the free surface. For reasons of comprehensiveness, we will give detail of their implementation in the following subsections.

2.1.1 Earth's Rotation

Hurricanes can cover large areas up to 100s or 1000s of km^2. On large geographic scale, Earth's rotation has a non-negligible influence on water circulation. In the presented model, this Coriolis forcing $\boldsymbol{\tau}_C$ is of the form $\boldsymbol{\tau}_C = f \cdot (-hv, hu)^\top$, and $f = 2\omega \sin(\varphi)$ with φ the latitude and $\omega = 7.2921 \cdot 10^{-5} [rad\ s^{-1}]$ the rotation rate of the Earth. A common approximation of the Coriolis force is the β-approximation, i.e. we linearly approximate $f = f_0 + \beta y$, where $f_0 \in \mathbb{R}$, y is a planar coordinate and $\beta \approx \frac{2\omega}{r_E}$ is a constant that depends on the Earth's rotation and radius r_E. We will use both parameterisations, the conventional and the β-approximation in this study.

2.1.2 Bottom Friction

The bottom friction $\boldsymbol{\tau}_B$ is assumed to take on the form of a quadratic Manning law $\boldsymbol{\tau}_B = \frac{gn^2 \|\mathbf{u}\|_2}{h^{7/3}} h\mathbf{u}$, where n is a dimensionless roughness parameter that is directly related to the nature of the lake bed and will take on values between 0.001 and 0.01 depending on the specifics of the test case. The bottom friction depends on the prognostic variables $\mathbf{U}$. In coastal areas, numerical flow directions might be reversed during wave run up due to small fluid depths and a resulting large friction term. To ensure stability of the numerical result, we follow the split-implicit time stepping procedure in [20] to ensure that flow directions do not reverse within one time step.

2.1.3 Bathymetry and Well-Balancing

Non-linear interaction with bathymetry plays a crucial role in wave amplification. Special care has to be taken to prevent spurious waves caused by erroneous numerical approximations of bathymetry gradients. In this study, we solve the strong form, equation (3), of the equations which plays a crucial role in the following discussion. Well-balancing, i.e., preservation of the steady state at rest is a desirable property of numerical discretisations. The steady state at rest assumes bathymetry gradients to be the only present source term. While well-balancing is achieved by setting gravity to zero in cells adjacent to the wet/dry interface [37], the strong form is well-balanced on a discrete level without any modification when the flux divergence $\nabla \cdot \mathbf{F}(\mathbf{U})$ is discretised after differentiation, since in general

$$\nabla \cdot \Big(\sum_k \big(\mathbf{F}(\mathbf{U}_k)\big) \phi_k(\mathbf{x}) \Big) \neq \sum_k \mathbf{F}_{div}(\mathbf{U}_k) \phi_k(\mathbf{x}). \tag{5}$$

where $\mathbf{F}_{div}(\mathbf{U}_k)$ and $\big(\mathbf{F}(\mathbf{U}_k)\big)$ are the nodal coefficients of the divergence of the flux and the flux, respectively. Since edge-based terms are always balanced, we show that for every wet element Ω_i we obtain

$$\mathbf{F}_{div}(\mathbf{U}_k) = S(\mathbf{U}_k). \tag{6}$$

for $\mathbf{u} = \mathbf{0}$. Equation (6) is fulfilled as long as the flux divergence and the source evaluated at the Lagrange points are balanced. This will always be the case in fully wet cells for the lake at rest where $\mathbf{u} = \mathbf{0}$, as

$$\mathbf{F}_{div}(\mathbf{U}_k) = (0, h_k\ \nabla h_k)^\top = (0, -h_k\ \nabla b_k)^\top = S(\mathbf{U}_k),$$

always holds true for all degrees of freedom k. This balance is not achieved if the order of differentiation and discretisation of $\nabla \cdot \mathbf{F}(\mathbf{U})$ are reversed. This can be easily shown by a counter example on a master element with edges $(-1,-1), (-1,1), (1,-1)$ and using linear Lagrange polynomials.

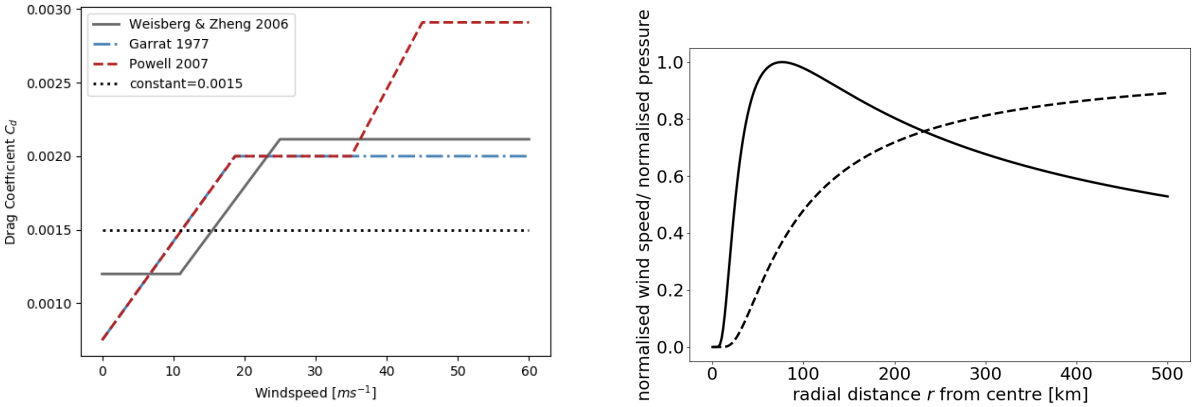

Figure 2: Wind drag coefficients c_d for hurricane storm surge models (left), Normalised wind speed (solid line) and pressure (dashed line) profiles using Holland's model (right). Wind speeds are normalised by $\mathbf{v}_{max} = \max_x \mathbf{v}$ and pressures by $p_n - p_c$.

2.1.4 Wind Fields and Wind Drag Coefficients

The wind stress is $\boldsymbol{\tau}_W = \gamma_\tau \boldsymbol{\tau}$ with a wind friction $\gamma_\tau \in \mathbb{R}_+$ that models the energy transfer from the atmosphere to the ocean. Given an external wind field $\mathbf{v}$, the wind stress can be computed as

$$\boldsymbol{\tau}(\mathbf{v}) = c_d \rho_a |\mathbf{v}| \mathbf{v}(\mathbf{x}, t) \tag{7}$$

where $c_d \in \mathbb{R}$ is a drag coefficient and ρ_a is the air density which we assume to be 1.15 $[kg\ m^{-3}]$. The drag coefficient $c_d = c_d(\mathbf{v})$ depends on wind speeds. For hurricane models several different wind drag parameterisations have been explored and commonly used ones are depicted in Figure 2 (left). In Garrat, 1977 [13] (blue line) observations from the past 10 years are used to show that for absolute wind speeds $|\mathbf{v}|$ within a range of 4 to $21 ms^{-1}$ the drag coefficient fulfils a linear relationship $c_d \cdot 10^3 = 0.75 + 0.067|\mathbf{v}|$ or a power law of the form $0.51|\mathbf{v}|^{0.46}$. In Weisberg & Zheng, 2006 [38] (gray line) a drag coefficient as in [23] is used to study sensitivities with respect to approach speed, direction of approach and landfall location (see also subsection 3.4 of this manuscript). Finally, Powell, 2007 [30], discusses wind drags for more extreme winds $|\mathbf{v}| > 50 ms^{-1}$ and numerically computes drag coefficients that exceed those known in the literature. Their new drag coefficients show improved results for practical applications.

2.1.5 Atmospheric Pressure

The atmospheric pressure gradient ∇p_A models part of the influence of the atmosphere onto the water column. In areas of relatively low air pressure in comparison to the ambient air pressure this causes the water surface to slightly bulge upwards, increasing h in this area. The influence of the pressure gradient is non-negligible: Numerical observation show that about 10% of the resulting surge can be attributed to the pressure gradient. It is implemented in a straight forward manner, utilising the local derivatives of the Lagrange polynomial expansion.

2.2 Adaptive Mesh Refinement

The computational model as described at the beginning of this section 2 uses the mesh generator `amatos` [7] to create dynamically adaptive and conforming triangular meshes. Smaller triangles are obtained by bisection [32]. The dynamic grid manipulation involves problem-dependent refinement indicators η_{Ω_i}, such as the gradient of the water height at time t

$$\eta_{\Omega_i}(t) = \max_{\mathbf{x} \in \Omega_i} \|\nabla H(\mathbf{x}, t)\|_2$$

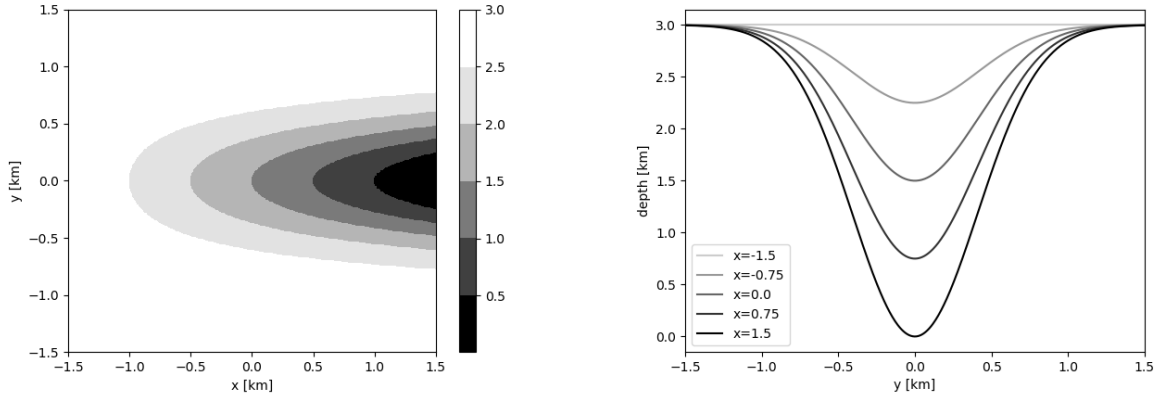

Figure 3: Hypothetical Embayment: 2D plot of bathymetry profile (left) and cross sections (right).

for each element Ω_i [5], to control the element-wise refinement or coarsening. Moreover, user-defined tolerances $0 \leq \theta_{\text{crs}} < \theta_{\text{ref}} \leq 1$ determine the fraction of the domain to be modified as follows:

$$\begin{array}{lll} \text{if} & \eta_{\Omega_i} \leq \theta_{\text{crs}} \eta_{\max} & \rightarrow \text{coarsen element } \Omega_i \\ \text{if} & \eta_{\Omega_i} \geq \theta_{\text{ref}} \eta_{\max} & \rightarrow \text{refine element } \Omega_i, \end{array} \tag{8}$$

with $\eta_{\max} = \eta_{\max}(t) = \max_{\Omega_i \subset \Omega} \eta_{\Omega_i}(t)$ the maximum value of the refinement indicator over all elements at time t.

The node values are then interpolated or restricted after modification using the known Lagrange basis functions for each element. In regions close to the waterline, we keep the mesh relatively fine (see also section 3.4) to avoid well-balancing issues. The refinement process has the further advantage of using a cache-efficient space-filling curve-ordering of elements [6], which allows fast access of neighbouring elements: This feature is particularly beneficial for local numerical discretisations such as discontinuous Galerkin method since elements only communicate over edges.

For convenience, the meshes are kept conforming, i.e. free of hanging nodes, throughout the simulation. We stress that this is not required by the method itself. Hanging nodes would require to combine two or more Riemann solutions over one (coarse) edge as was recently demonstrated [14, 21].

3 Results

In this section, we present test cases to show the major functionalities of the model. Note, that physical dimensions are not explicitly given, but we assume throughout this paper that we are using SI units. The following subsections will in particular focus on the aspects of:

- Inundation stability and conservation properties (section 3.1);
- Balanced wind and pressure forcing (section 3.2);
- Robustness of wind forcing (section 3.3);
- Idealized storm surge modelling and sensitivity analysis (section 3.4)

3.1 Tidal Flow in a Symmetric Embayment

Here, we show one configuration of the simulation of an embayment first presented in [18]. See also [25] for simulation results with the finite element model ADCIRC and [11] for another discontinuous Galerkin simulation with a modified bathymetry. This simulation is to show idealised estuarine flooding by an in- and outgoing tide to show inundation stability and conservation properties of the model. On a square domain $\Omega = [-L, L]^2$ with $L = 1500$ a symmetric bathymetry as shown in Figure 3 is defined by $b(\mathbf{x}) = 3.0 - (1.50 + \hat{x})\mathrm{e}^{-3\hat{y}^2}$, where we use the definition $\hat{x} = 10^{-3}x$, $\hat{y} = 10^{-3}y$. Moreover the water surface is assumed to be in a steady state at rest. On the right boundary of the domain (at $x = L$), a

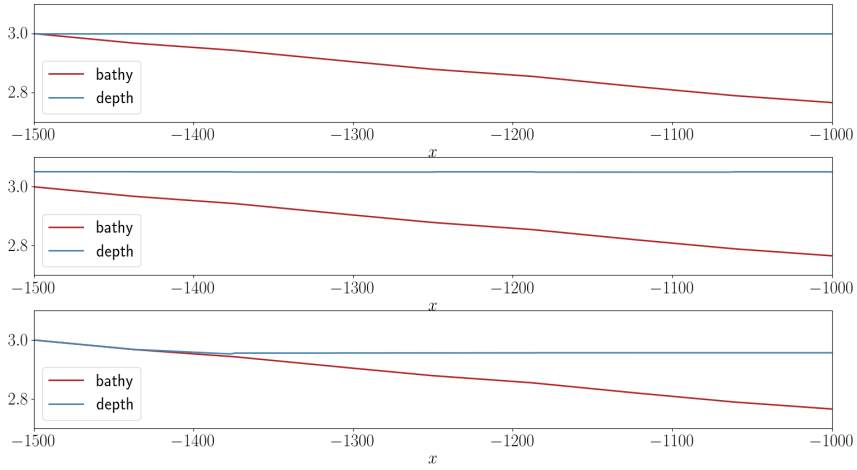

Figure 4: Hypothetical Embayment: Cross sections of the solution for $x \in [-1500, -1000]$ projected onto $y = 500$ at times $t = 0, 31.1$, and 62.1 hours (top to bottom).

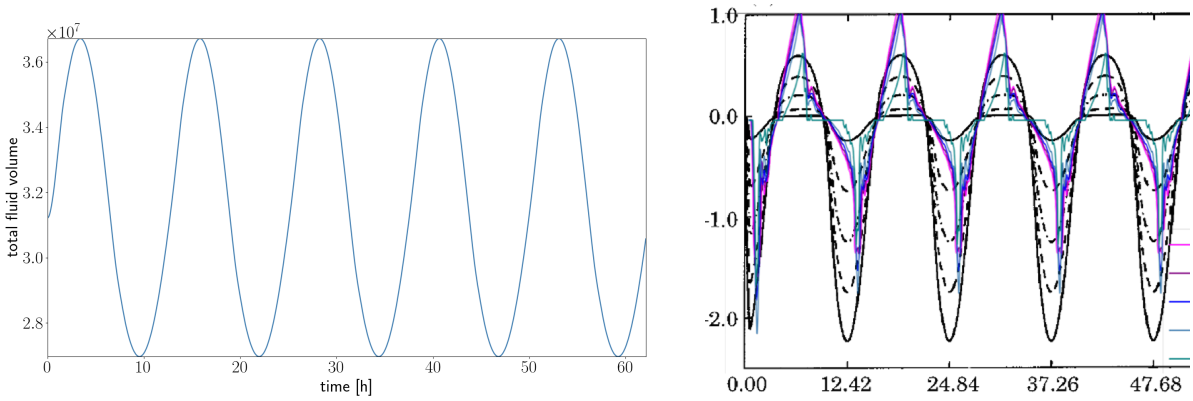

Figure 5: Hypothetical Embayment: Plot of fluid volume (left) and comparison of integrated flux Hu (coloured lines) with the results presented in Ip et al., 1998 (black lines) for four full tidal cycles over cross sections at $\hat{x} \in \{0, \pm 0.6, \pm 1.2\}[km]$ (right) over time.

tidal forcing is prescribed as

$$H(\mathbf{x}, t) = h_{\text{de}} + 3 \sin\left(\frac{2\pi t}{T}\right),$$

for $x = L, y \in [-L, L]$, where T is the M_2 tide, i.e. a temporal period of $T = 12.42[h]$ is prescribed [18] and h_{de} denotes the water depth in the deepest end of the domain. All other boundaries are set to be reflecting. Friction is assumed to be negligible, i.e., $n = 0$. For the initial water surface, we define a lake at rest such that the water surface is level with the highest point of the bathymetry $b_{max} = 3.0$.

To avoid polluted results caused by the definition of the boundary condition, we artificially increased the domain by L to the right, i.e., for $\hat{x} \geq 1.5$, and assume the bathymetry in this area to be identically zero, hence adding a discontinuity to the bathymetry. As we will see this did not pose a problem to our robust numerical method. We ran five full tidal cycles with a time step of $\Delta t = 4[s]$, a spatial resolution of $\Delta x = 93.75[m]$ and a CFL number of around $\frac{1}{3}$ which we found to be the largest possible CFL number for this particular test case that allowed for a stable computation and which is similar to the maximal CFL numbers found in [39] for similar applications. The determination of theoretical bounds for CFL numbers for multi-dimensional problems is difficult and most results are restricted to one space dimension [22]. Snapshots of the numerical solutions over a cross section at $y = 500$ can be found in Figure 4 which shows that wetting and drying is occurring on the left boundary of the domain and hence, that the inundation

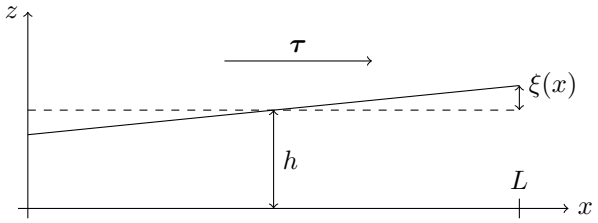

Figure 6: Steady State Wind Test Case: 1D projection of the initial conditions. In this figure, z denotes a vertical coordinate.

x $[m]$	500.00	10500.00	20500.00
$\xi(x)$ $[cm]$	-2.04	0.00	2.04

Table 1: Steady State Wind Test Case: Analytical solution at discrete points $x \in \{500, 10500, 20500\}$.

scheme is stable. We observe – see left display in Figure 5 – global mass conservation in agreement with [18] showing that the limiter presented in [37] is non-destructive with respect to global mass conservation and that the variation of total fluid volume due to the tidal in/outlet is of the order of $\mathcal{O}(10^7)$. We note that the model used in [18] achieves a much larger time step of $\Delta t = 111.78s$ at a spatial resolution of $\Delta x = 75[m]$. We attribute this to the fully implicit evolution scheme that their model uses. Furthermore we numerically computed the integral of the flux Hu over cross-sections at $x \in \{\pm 1200, \pm 600, 0\}[m]$:

$$\int_{-\omega}^{\omega} (h+b)(\tilde{x}, y) \cdot u(\tilde{x}, y)\ dy$$

The results are shown in the right display of Figure 5. We see that after a short calibration time, the results match the results in [18] well (see also Figure 5 (right)) and yield values for the cumulative transport of the order 10^3. We note that especially at $\hat{x} = -1.20$ we still get meaningful and non-zero results. This is notable because that part of the domain is close to the left hand boundary and therewith exposed to wetting and drying (see Figure 4 for a close-up) and shows that the slope limiting strategy is gentle enough to reduce spurious oscillations while also yielding realistic values for velocities. Finally we point out that the results are found to not be sensitive to the parameter ϵ_{tol} that determines a cut off value for small water depths. We ran the simulation with $10^{-6} \leq \epsilon_{tol} \leq 10^{-3}$ and did not find different results.

3.2 Steady State Wind Test Case

This test case was described in [10]. In a rectangular basin $\Omega = [0, L] \times [0, D]$ with dimensions $L = 21[km]$ and $D = 5[km]$ with constant bathymetry $b(\mathbf{x}) = 0$, reflecting boundaries on all four edges, a linear water surface $h_d + \xi$ is described as shown in Figure 6. Here, $h_d = 5[m]$ and

$$\xi(\mathbf{x}) = \frac{\tau_1}{g h_d \rho} \left(x - \frac{L}{2} \right),$$

with g the acceleration due to gravity, $\rho = 10^3[kg\ m^{-3}]$ the water density, and absent initial velocities $\mathbf{u} = \mathbf{0}$. A constant wind stress is assumed as $\boldsymbol{\tau} = (\tau_1, \tau_2)^\top = (0.1, 0)^\top$ and $\gamma_\tau = 1$. In previous studies [10, 31] the steady state is described as shown in Table 1. The main balance here is to be achieved in the x-momentum equation between the flux divergence $\nabla \cdot \mathbf{F}(\mathbf{U})$ and the wind stress, i.e.

$$g(h_d + \xi) \frac{\partial}{\partial x} \xi(\mathbf{x}) \stackrel{!}{=} \frac{1}{\rho} \tau_1(\mathbf{x}), \tag{9}$$

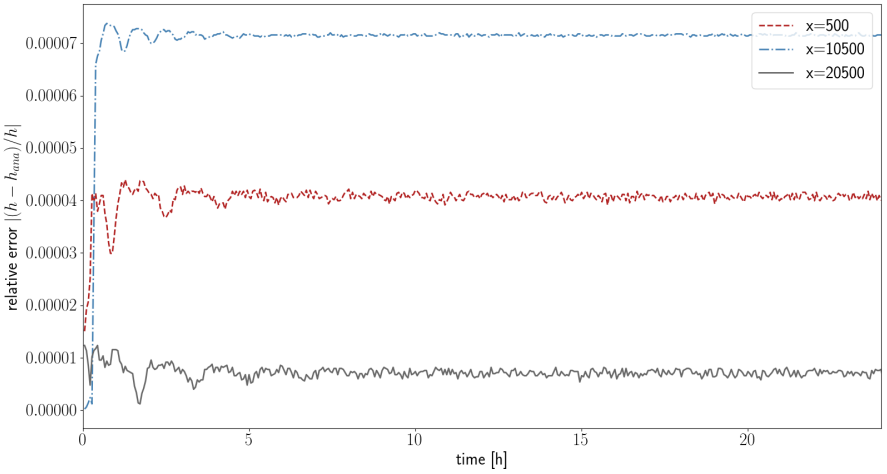

Figure 7: Steady State Wind Test Case: Relative error at $x = 500$ (solid line), $x = 10500$ (dashed line) and $x = 20500$ (dashed dotted line).

on a discrete level. The partial derivative of ξ can be computed as $\frac{\partial}{\partial x}\xi(\mathbf{x}) = \tau_1(gh_d\rho)^{-1}$ as ξ is a linear function of x. Subbing in the derivative of ξ and $\tau_1 = 0.1$ in equation (9), we get after division by g:

$$(h_d + \xi) \cdot \left(\frac{0.1}{gh_d\rho}\right) = \frac{0.1}{g\rho} \Leftrightarrow (h_d + \xi) = h_d.$$

This equality is approximately satisfied because $\xi \ll h_d$ by definition, i.e., $\frac{h_d+\xi}{h_d} \approx 1$.

For the simulation we used a time step of $\Delta t = 10[s]$ and a Runge Kutta time stepping scheme of third order (RK35) until $T_{end} = 10^4 s$ with a spatial resolution of $\Delta x = 656.3[m]$ and a CFL number of 0.2246 which is close to the theoretical maximum and was found to lead to stable results. The Manning friction does not have a significant impact in this case as the numerical velocities are negligible. The results are shown in Figure 7. Depicted are the relative errors in surface height h at the numerical wave gauges at $x \in \{500, 10500, 20500\}$ over time. We observe that a steady state is reached after about 8 hours which we attribute to the reflecting boundary conditions in our simulation. This is in contrast to the findings in [10] who solved RANS equations with horizontal and vertical eddy viscosities to achieve an exact solution. The reason for this is that their model allowed the definition of an eddy viscosity of the form $A_H\Delta\mathbf{u} = A_H\nabla^2\mathbf{u}$ and a boundary condition of the form $\partial_z A_v \partial_z \mathbf{u}$ at the free surface. By setting $A_v u_z = \tau/\rho$ they achieve an exact balance of the wind field and the gradient leading to an exact solution. Overall, we see that the steady state values from Table 1 are matched and the wind and gravity forces are balanced. Our observed relative errors are of the order $\mathcal{O}(10^{-5})$ and are decreasing with increasing spatial resolution. Figure 8 furthermore shows snapshots of the numerical solution over the cross section at $y = 2500$ at discrete time steps. Shown are the fluid height and velocities for every $500s$ in light grey and for $t = 0, T_{end}/2, T_{end}$ in colour. We observe that due to the boundary conditions small meridional velocities $\mathbf{u} = (u, v)^\top$ form at the walls at ($x = 0$ and $x = 21000$). However, they stay bounded throughout the simulation, do not influence the surface height h significantly and do not destroy the steady state balance. We attribute this to enough numerical diffusion being present in the model that disperses energy and prevents build-up.

3.3 Wind-Induced Circulation in a Semi-enclosed Homogeneous, Rotating Basin

This test case is described in [33]. In a semi-enclosed rectangular domain $\Omega = [0, 10D] \times [0, D]$ with $D = 10{,}000$, a piecewise linear bathymetry (see also the sketch in Figure 9) of depth $h_{\max} \in \mathbb{R}$ is prescribed as follows:

$$b(\mathbf{x}) = \frac{2(h_{\max} - h_0)}{D}\left|y - \frac{D}{2}\right|.$$

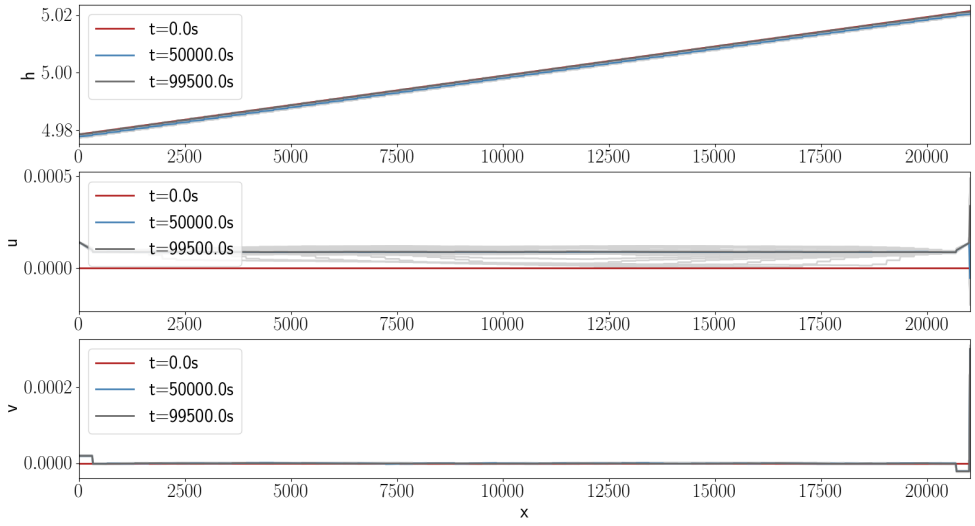

Figure 8: Steady State Wind Test Case: Surface elevation (top), meridional velocities (middle and bottom) at cross section $y = 2500$ at times $t \in [0, T_{end}/2, T_{end}]$ in color and for all other times in between in light gray.

Here, $\mathbf{x} = (x, y)^\top$ is the spatial coordinate and $h_0 = 3$ $[m]$ is the minimum water depth. The water surface is at rest at time $t = 0$ and a constant wind stress $\boldsymbol{\tau} = (\tau_C, 0)^\top$, $\tau_C \in \mathbb{R}$, aligned with the x-axis is prescribed and linearly ramped up over a period of 6 hours. Six different configurations of the

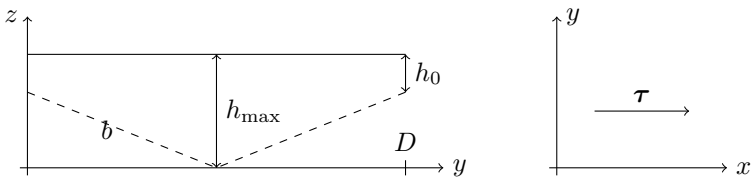

Figure 9: Wind-Induced Circulation in a Semi-enclosed Homogeneous, Rotating Basin: Sketch of initial condition. Depicted are the bathymetry and initial water surface (left) and the wind field (right).

parameters, that are given in Table 2, were tested to assess how the maximal occurring velocities are impacted by rotation, strength of the wind stress $\boldsymbol{\tau}$, as well as depth of the basin $h_{\max}$.

We show simulation results on a uniform grid using 81920 triangular linear elements with radii of the inscribed circles of about $\Delta r = 38.5$. This corresponds to a spatial distance of $\Delta x = 781.25$ and $\Delta y = 156.25$ between grid points. On the left most edge of the basin, we used transparent boundary conditions. Reflecting boundary conditions are prescribed on all other boundaries. A quadratic Manning law with $n = 0.0025$ as was suggested in a previous study [33] and was used to parameterise the bottom friction and a β-approximation to model the Coriolis forcing as described in subsection 2.1.1 was used with $f_0 = 0.001$.

The results can be found in Figure 10. For all six configurations the magnitude of the velocities are plotted in color as well as the velocity vectors for every 100th point. Note that configurations 5 and 6 are scaled by factors of 10 and 0.2 respectively to improve readability. Figure 11 shows cross-sections of velocities (scaled with the maximum occurring velocity) at $x = 50$ km (mid basin) and $x = 98$ km (close to the head of the channel located at $x = 100$ km). In general, we observe a re-circulation zone of below 10km from the head which is in line with the observations reported in [33]. The major characteristics of this test case are reproduced by the simulation results: We find a positive correlation between wind strength and velocities (two bottom panels of Figure 10) as well as a negative correlation between water

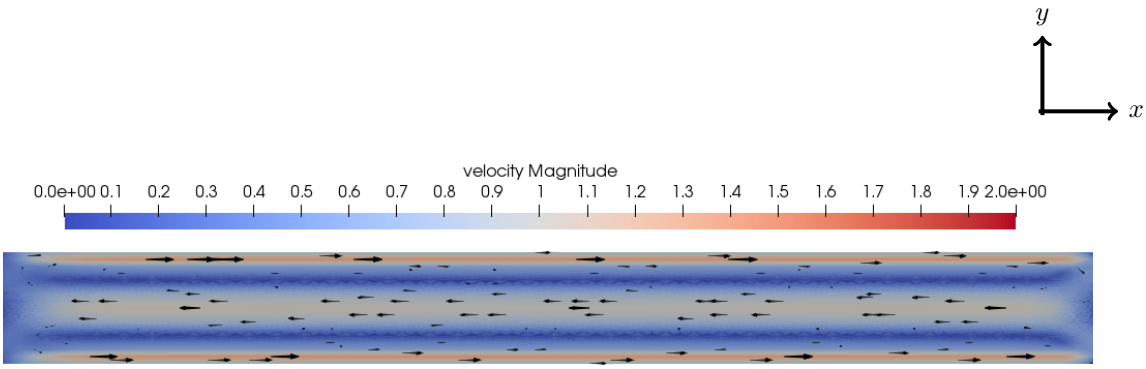

(a) Configuration 1

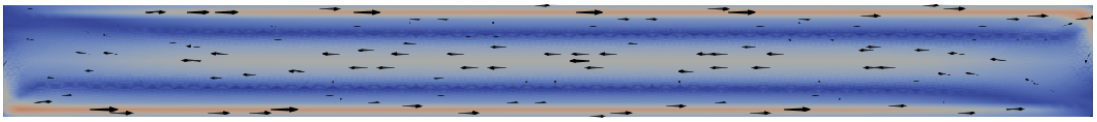

(b) Configuration 2

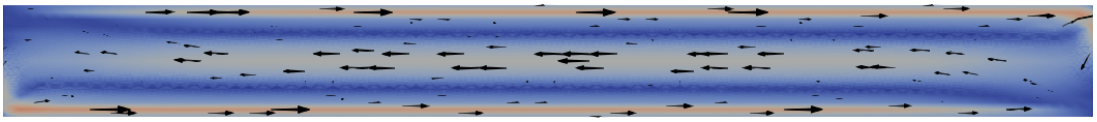

(c) Configuration 3

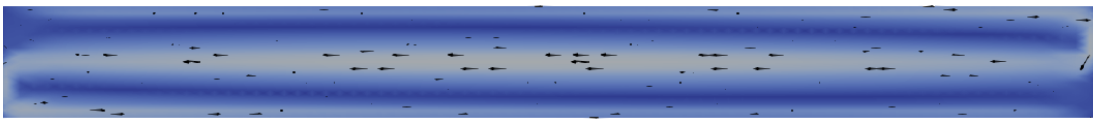

(d) Configuration 4

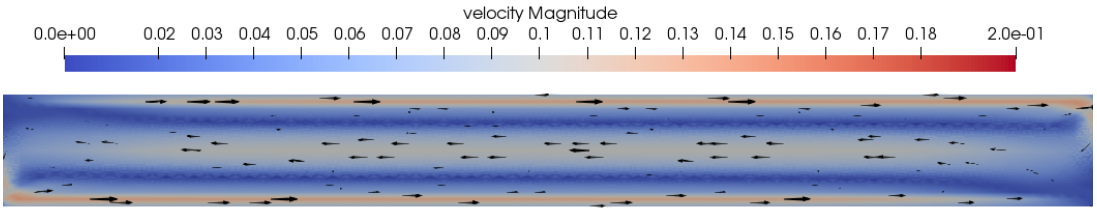

(e) Configuration 5

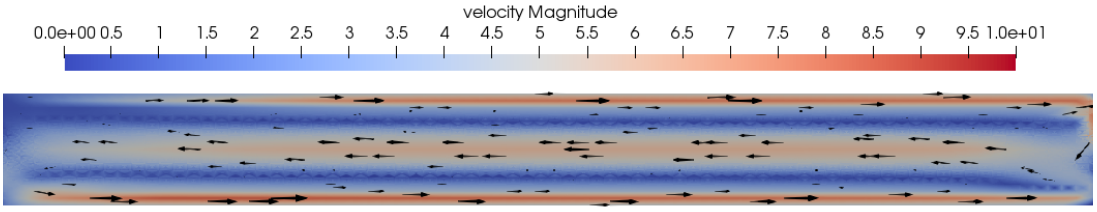

(f) Configuration 6

Figure 10: Wind-Induced Circulation in a Semi-enclosed Homogeneous, Rotating Basin: Velocities for all configurations (1–6) at time $t = 37500[s]$ (top to bottom).

Experiment Number	$\tau_C[Pa]$	$f_0[s^{-1}]$	$h_{\max}[m]$
Configuration 1	0.080	0	20
Configuration 2	0.080	10^{-4}	20
Configuration 3	0.080	10^{-4}	60
Configuration 4	0.080	10^{-4}	8
Configuration 5	0.008	10^{-4}	20
Configuration 6	0.500	10^{-4}	20

Table 2: Wind-Induced Circulation in a Semi-enclosed Homogeneous, Rotating Basin: Parameters for all six experiments.

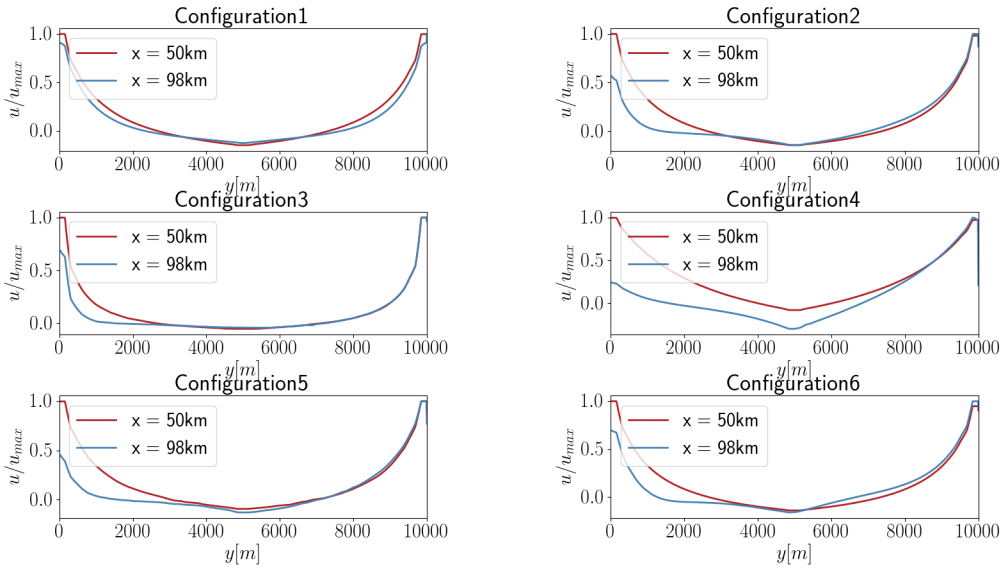

Figure 11: Wind-Induced Circulation in a Semi-enclosed Homogeneous, Rotating Basin: Scaled velocities at $t = 20000[s]$.

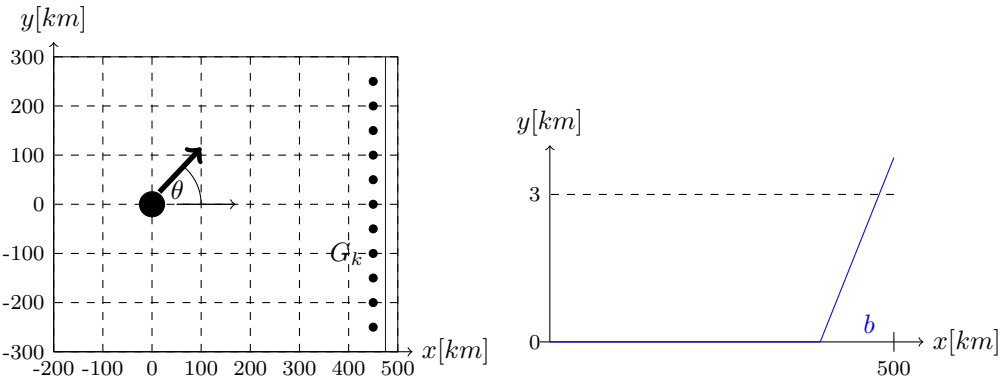

Figure 12: Idealised Hurricane Approaching a Linearly Sloping Coast: Top down view of set up with beach indicated by blue line, wave gauges by dots, the initial storm position by a large black dot, and the approaching angle with θ (left); cross section of bathymetry (blue line) and resting water surface (dashed line) (right).

Configuration	start point in [km]	approaching angle θ	approaching speed
1	$(0.0, 0.0)^\top$	$0°$	$5ms^{-1}$
2	$(200.0, -100.0)^\top$	$-45°$	$5ms^{-1}$
3	$(200.0, 100.0)^\top$	$45°$	$5ms^{-1}$
4	$(425.0, -100.0)^\top$	$-90°$	$5ms^{-1}$
5	$(425.0, 100.0)^\top$	$90°$	$5ms^{-1}$
6	$(0.0, 0.0)^\top$	$0°$	$25ms^{-1}$

Table 3: Idealised Hurricane Approaching a Linearly Sloping Coast: Parameters for all six experiments

depth h and the magnitude of the velocities $|\mathbf{u}|$. For the non-rotational case (Configuration 1, top panel in Figure 10), we agree with the observations from [33] and find a symmetric profile of the meridional velocities. This changes for all rotational test cases in which we find asymmetries near the head (at $x = 98km$ – see Figure 11). We furthermore find (see Figure 11) steeper gradients on the left shoal for configurations 2 and 3. For configuration 4, [33] find a symmetric velocity profile – almost as for configuration 1 – this, we cannot confirm. However, we would like to point out that they used different equations to model this problem. Hence, an explanation might be found, again, in the characteristics of the shallow water equations. They are depth-integrated, so that the Coriolis force effects the entire water column. The model employed in [33] used between $10 - 30$ vertical layers in their model which we believe to add a dissipation that we are unable to reproduce.

Resolution appears to be a critical issue for this test case. With a spatial resolution of only $\Delta r = 154$ (a total of 5120 triangles in Ω) we observe that after long integration times instabilities develop in the form of vortices at the bottom end of the domain for all rotational configurations (2–6), indicating that the resolution is not sufficient for a realistic and physically correct solution. We attribute this effect to the depth-integrated character of the shallow water equations as well as the occurrence of a geostrophic imbalance. As opposed to the model used in [33] that included several vertical layers and with that the ability to dissipate energy in the vertical dimension resulting in a rotation of the fluid in the (y–z)-plane, the depth integrated shallow water equations cannot take vertical motion into account.

3.4 Idealised Hurricane Approaching a Linearly Sloping Coast

In order to study the viability of the current model for use in hindcasts, we implemented an idealised test which is similar to a test presented in [27]. It is designed to reproduce observations of a published sensitivity study [38]. The latter showed that hurricane flood intensity is sensitive to the storm's approach speed, direction of approach θ, and landfall location. Our idealised test set up is defined as follows:

Let $\Omega = [-200, 500] \times [-300, 300]\ km^2$ be a rectangular basin with a transparent boundary at $x =$

$-200[km]$, reflecting boundaries otherwise and a bathymetry defined by the piece-wise linear function

$$b(\mathbf{x}) = \begin{cases} 0 & \text{for } x \leq 350km \\ \alpha_b \cdot (x - 350km) & \text{otherwise,} \end{cases}$$

where $\alpha_b = 0.025$ is the slope of the bathymetry, $\mathbf{x} = (x, y)^\top$ is the spatial coordinate (see also Figure 12). The initial water surface is at rest and described by $h(\mathbf{x}, 0) = \max(3.0 - b(\mathbf{x}), 0.0)$. Note that we used km for the definition of the initial heights to improve readability.

We then initialise a cyclone at an initial position (see large black dot in Figure 12) and an approach angle θ. The corresponding wind stress $\boldsymbol{\tau}$ requires the computation of a continuous wind field. This can either be accomplished by using re-analysis data or a parameterised model that allows the derivation of a continuous wind field from a few discrete parameters; [8] for a short discussion on using a parameterised model in combination with re-analysis data for the Republic of Ireland. In the present model, the wind field is computed using a parameterised model [16], which we elaborate on in more detail in subsection 3.4.1, with parameters $p_c = 950.0$, $p_n = 1005.0$, $A = 23$ and $B = 1.5$ which are representative for the 2008 hurricane Ike. Six different configurations as in [27] are implemented (cf. Table 3) and final times T_{end} are chosen such that the storm's landfall is captured. Note, that we use oceanographic conventions, i.e. 0° corresponds to travelling to the right. The boundary conditions are transparent at $x = -200km$ and reflecting otherwise. Transparent boundaries for this sub-critical flow were implemented following [2] using a standard approach based on Riemann invariants.

3.4.1 Holland's Model to Compute Hurricane Winds

The wind stress in equation (7) depends quadratically on the wind $\mathbf{v}$. For hurricanes, winds can be computed using the model [16]:

$$\mathbf{v}(\mathbf{x}) = v(r) \cdot \mathbf{t} \quad \text{with} \quad v(r) = \sqrt{\frac{AB(p_n - p_c)e^{-\frac{A}{r^B}}}{\rho_a \rho r^B} + \frac{r^2 f^2}{4}} - \frac{rf}{2},$$

where r is the distance from the centre of the storm, $\mathbf{t}$ the tangent to the circle with radius r, $A, B \in \mathbb{R}$ are shape parameters, p_n, p_c are the ambient and central pressure respectively, ρ the water density, and f the Coriolis parameter. The parameters A and B are then obtained from the maximum wind speed as well as the radius of maximum winds (RMW):

$$B = (\max |\mathbf{v}|)^2 / \Delta p \cdot (\rho_a e) \quad \text{and} \quad A = \text{RMW}^B, \tag{10}$$

where e is Euler's number. An example for a normalised wind profile can be found in Figure 2. The wind model [16] also gives a corresponding atmospheric pressure

$$p_A = p_c + (p_n - p_c)e^{\frac{-A}{r^B}},$$

as can be seen from Figure 2 (right) which shows pressures (dashed line) normalised by $p_n - p_c$ as well as wind speeds normalised by $\max |\mathbf{v}|^2$.

3.4.2 Numerical Results

We ran the simulation with a constant time step of $\Delta t = 10[s]$ at a CFL number of around 0.183 with a spatial resolution of $\Delta x = 10.9375[km]$, a Manning parameter of $n = 0.001$, and the wind drag as in [38]. We then compared the signal at numerical wave gauges G_k located at $G_k \cdot 10^{-5} = (4.5, -2.5 + 0.5k)^\top$ for $k = \{0, 2, 4, \ldots, 20\}$ (see left display of Figure 12) with the findings in [27] and found overall good agreement. The results can be found in Figure 13. It shows the water wave signal for all six Configurations obtained at the numerical wave gauges G_k for all even numbered wave gauges with the amplitudes plotted in metre $[m]$ with a vertical offset of $10 \cdot k$ for gauge G_k to increase readability. In agreement with the literature [38] we find that the observed flooding is sensitive to the approaching angle. The plots for Configurations 2 and 3 in Figure 13 show significantly different signals at the wave gauges to the left and right of the wave gauge at which the storm made landfall. They differ in shape and arrival time. The general N-shape of the largest waves as seen in [27], however, could not be reproduced. An investigation showed the N-shape could be reproduced with a bathymetry with slope $\alpha_b = 0.0125$, which corresponds to an entirely wet domain. Since higher resolution simulations with a halved Δx showed the same

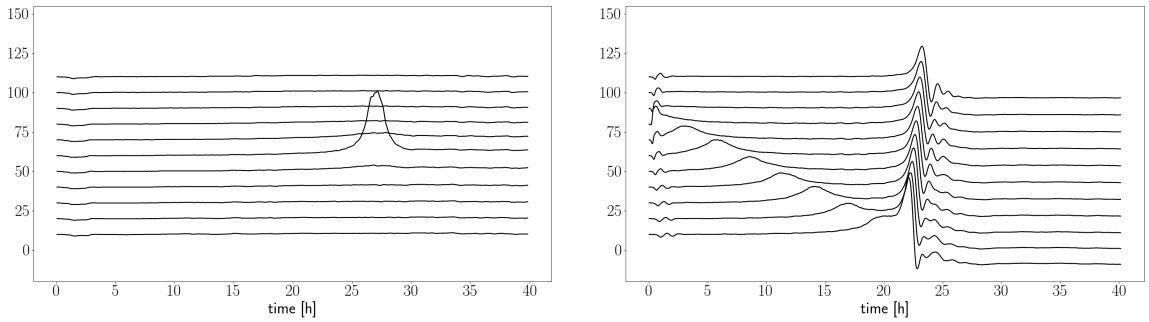

(a) Configuration 1

(b) Configuration 4

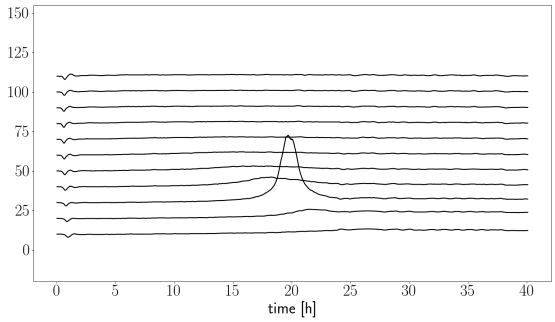

(c) Configuration 2

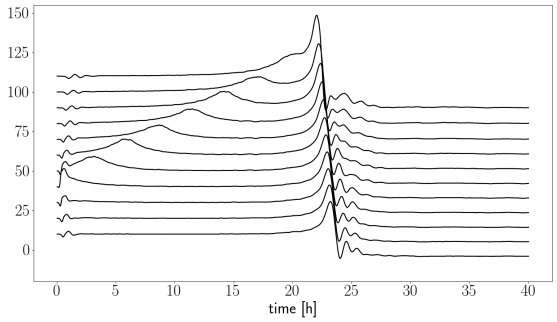

(d) Configuration 5

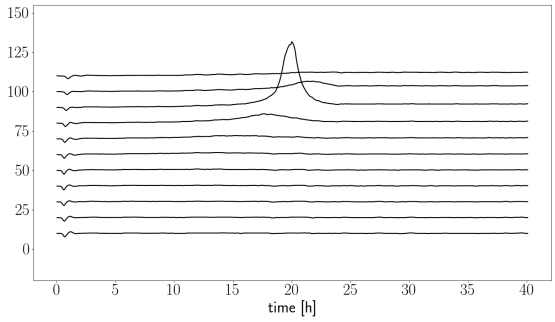

(e) Configuration 3

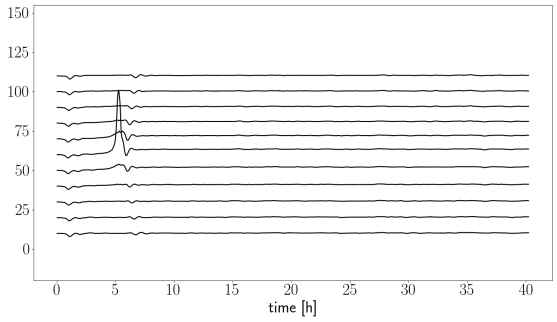

(f) Configuration 6

Figure 13: Idealised Hurricane Approaching a Linearly Sloping Coast: Waterfall Plot of Time series at even numbered wave gauges from bottom to top for all six configurations. Amplitudes are in m with an added offset of $10 \cdot k$ for wave gauge G_k for all k.

Ramp Up Time	15min	30min	1h	2h	4h
η_{max} at G_{10}	41.400	41.400	41.700	41.600	41.700
η_{max} at G_{12}	6.500	6.400	6.500	6.300	6.500
η_{max} at G_{20}	2.300	2.200	2.200	2.300	2.400

Table 4: Idealised Hurricane Approaching a Linearly Sloping Coast: Maximum wave height η_{max} in cm with respect to ramp up time at gauges G_{10}, G_{12}, and G_{20}.

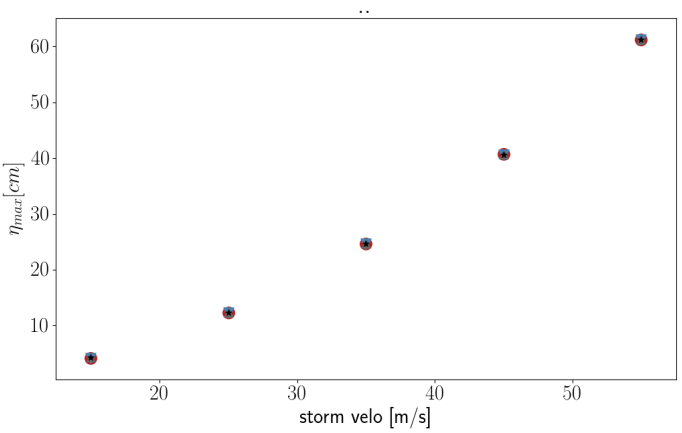

Figure 14: Idealised Hurricane Approaching a Linearly Sloping Coast: Maximum wave height η_{max} versus maximum wind speed, $\max \mathbf{v}$, for different drag coefficients (red dots - Weisberg & Zheng, blue upside down triangles - Powell, grey triangles - Garrat and black stars - constant.

behaviour, we attribute this effect to the implementation of reflecting boundary conditions in this test case. We furthermore remark that Configurations 4 and 5 in Figure 13 show a large second wave that we found to be caused by the reflecting boundary conditions in y direction as well.

3.4.3 Influence of Ramp Up Times and Robustness

Numerical models often require a gentle ramping up of source terms in order to reduce spurious oscillations and to allow for a robust computation. In our simulations, we ramped up the wind stress $\boldsymbol{\tau}$ and pressure p using an exponential blending in time. For early times $t \leq t_{ru}$ this filter $\mathcal{F}$ takes on the form

$$\mathcal{F}(\phi) = \phi \mathrm{e}^{-\left(\frac{t-t_{ru}}{c_f\, t_{ru}}\right)^2},$$

with ϕ the quantity that is to be started and c_f a tunable coefficient. The storm only starts travelling towards the coast with angle θ after the ramp up time t_{ru} is reached. Before, it is kept at its starting position, so that the wind and pressure fields are slowly ramped up until they reach their full strength. We ran Configuration 1 with five different ramp up times between 15 minutes and 4 hours (see also Table 4) to test the robustness of the results. Ideally, we would like t_{ru} to be as small as possible to save computing time but large enough to not pollute numerical results. We observe that for all times between 15 minutes and 4 hours we get robust numerical results. Furthermore, as can be seen from Table 4 the maximum wave height does not show a lot of variation depending on different ramp up times and the maximum variation is found to be 0.3cm.

3.4.4 Sensitivity with Respect to the Wind Drag Parameter c_d

Modelling the energy transfer from the atmosphere to the ocean surface is accomplished through a wind drag parameter c_d (a source term; see also equation (7)) that couples the external wind field to the hydrodynamic model. As described in section 2.1.4 several wind drag parameterisations have been developed in the literature. Exemplarily, we tested the set of four parameterisations described in section 2.1.4 for Configuration 1 in order to determine their influence on maximum wave heights at wave gauges G_k which we assume a good indicator for wave run-up at the coast. Table 5 shows maximum and minimum wave heights for the original Configuration 1 at selected wave gauges closest to the storm's landfall. We

Gauge No.		Weisberg & Zhang	Garrat	Powell	constant
10	$\eta_{max}[cm]$	41.600	41.600	41.600	41.700
	$\eta_{min}[cm]$	−10.000	−9.900	−9.800	−9.500
12	$\eta_{max}[cm]$	6.300	6.300	6.500	6.500
	$\eta_{min}[cm]$	−10.500	−10.500	−10.400	−10.000
20	$\eta_{max}[cm]$	2.300	2.300	2.400	2.400
	$\eta_{min}[cm]$	−8.100	−8.000	−7.900	−7.600

Table 5: Idealised Hurricane Approaching a Linearly Sloping Coast: Maximum and minimum wave height with respect to different drag coefficients at gauges G_{10}, G_{12}, and G_{20}.

Configuration	Δp [mbar]	$\max \lvert\mathbf{v}\rvert [m/s]$	RMW [km]	A	B
1a	46.0	50.0	10.0	50.11	1.7
1b	46.0	50.0	20.0	162.313	1.7
1c	46.0	50.0	47.0	695.931	1.7
1d	46.0	50.0	75.0	1533.171	1.7

Table 6: Idealised Hurricane Approaching a Linearly Sloping Coast: Holland parameters for storms of different sizes/ varying RMW.

repeated the simulation with all four different wind drag models and observe merely minor differences of the order of at most half a centimetre. The parameter $c_d = c_d(\mathbf{v})$ depends on the wind speed. Therefore, we ran Configuration 1 with varying maximum wind speeds $\max |\mathbf{v}| \in \{15, 25, 35, 45, 55\} ms^{-1}$ for every wind drag model. As shown in Figure 14 we see that the differences in maximum wave heights $\eta_{\max}$ are negligible. In fact, they are, again, of the order of at most half a centimetre. Hence, we conclude that in an idealised model such as the one presented in this manuscript different wind drag models do not lead to significantly different results. This can be explained by the form of the wind stress $\boldsymbol{\tau} = \rho_a c_d |\mathbf{v}| \mathbf{v}$. Using the selected parameterisations, c_d will differ at most by a factor of 2 in very localised regions of the storm, which does not lead to a significant increase or decrease in the observed wave heights close to the coast.

3.4.5 Influence of Storm Size

The size of a hurricane plays an important role in the observed flooding. For reasonable storm sizes a variability of about 30% in observed surge is reported [19]. In the wind model [16] the shape and size of the storm depend on the shape parameters A and B. These, in turn, depend on the radius of maximum winds (RMW), the difference between ambient and central pressure $\Delta p = p_n - p_c$, the air density ρ_a and the maximum wind speeds as shown in equation (10). Assuming storm conditions that are representative for the 2017 hurricane Ophelia, we simulate Configuration 1 as described above and vary the radius of maximum winds. According to [17], the average radius of maximum winds of hurricanes is $47km$, with a standard deviation of $27km$ which is why we chose to run simulations with the radii stated in the Table 6. As can be seen, only parameter A varies with varying RMW if all other conditions are kept fixed as it describes the radial scaling on the RMW and the location of the maximum wind relative to the origin. We measured the maximum wave height at wave gauge G_{10} – the location at which the synthetic storm made landfall – and will hence record the maximum surface elevation η_{max}. The results are depicted in Table 7. We see that with this simple parameterisation, we achieve measured maximum wave heights with a variability of about 39%. Given, that we tested with parameters resembling hurricane Ophelia for the most part, we conclude that we are within the range of variability that was found in [19].

	Configuration 1a	Configuration 1b	Configuration 1c	Configuration 1d
$\eta_{max}[cm]$	38.6	48.4	55.2	63.4

Table 7: Idealised Hurricane Approaching a Linearly Sloping Coast: Maximum wave height for different storm sizes at wave gauge G_{10}.

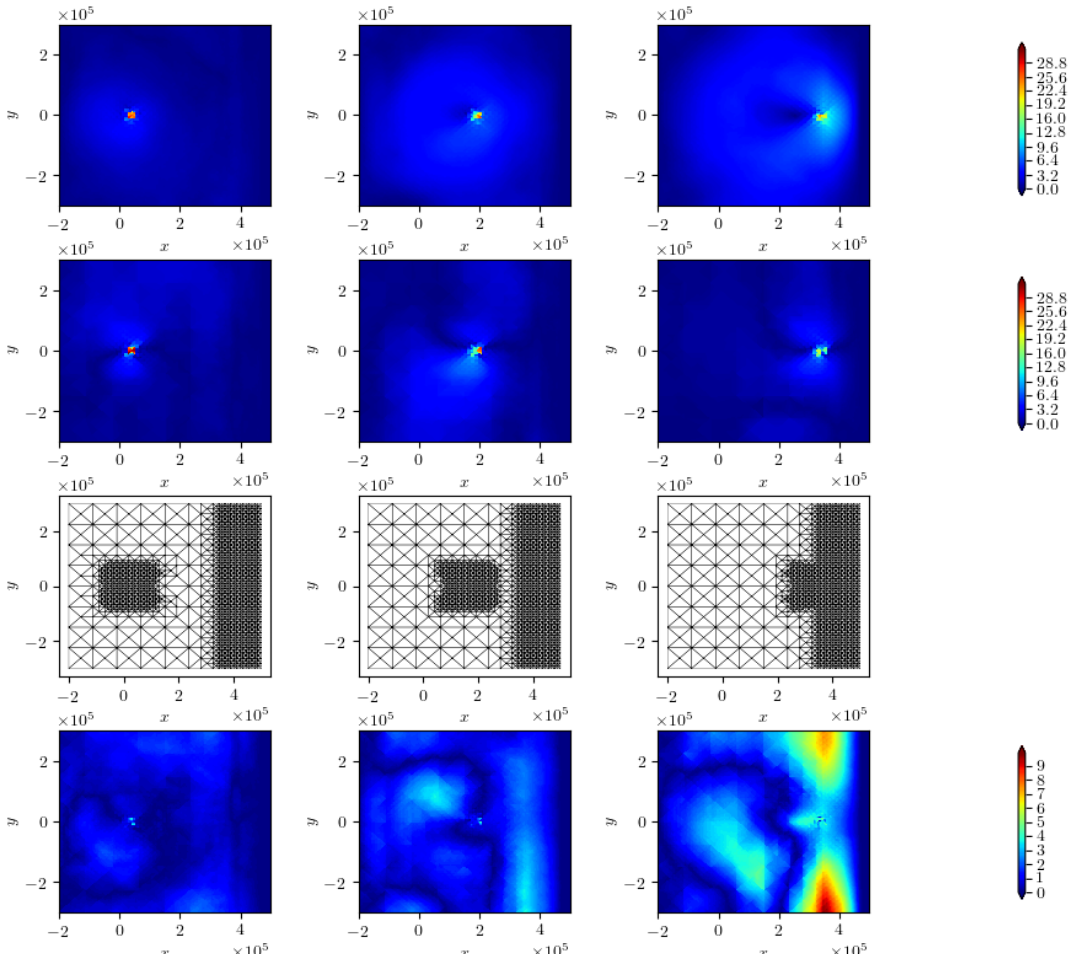

Figure 15: Idealised Hurricane Approaching a Linearly Sloping Beach: Simulation results at times $t = 0, T_{end}/2, T_{end}$ (left to right). Depicted are the current magnitudes of the uniform (top) and adaptive (top middle) simulation; the adaptive meshes (bottom middle) and absolute difference between both simulations (bottom).

3.4.6 Adaptive Simulations

Dynamically changing non-uniform meshes as described in section 2.2 are ideal for simulating localised phenomena at a reduced computational cost. Since storm wave heights are strongly influenced by changes in bathymetry as well as the size and strength of a storm, we define a refinement indicator η_{Ω_i} to take both of them into account for every element Ω_i:

$$\eta_{\Omega_i} = |\nabla b|_{2,\Omega_i} + |\mathbf{v}|_{2,\Omega_i}. \tag{11}$$

Using the indicator (11), we achieve a refinement of the beach or bathymetry gradient as well as the storm position (see Figure 15). Figure 15 shows numerical results for Configuration 1 on an adaptive and a uniform mesh. Plotted are the non-uniform meshes and currents at times $t = 0, T_{end}/2, T_{end}$. We can see that the adaptive and uniform simulations yield comparable results and that differences are generally low. We remark though that on landfall currents are mis-estimated for the not refined region which we attribute to the limiting strategy employed to stabilise the simulation. This, however, does not impact the measured wave heights near the coast. The maximum wave heights measured at gauges G_k are depicted in Figure 16 and show good agreement between the adaptive and uniform simulation. Although dynamic mesh refinement adds computational overhead, this was not found to be significant. The uniform simulation comprised 8192 elements, while the adaptive simulation only used on average: 2714 (and a maximum 3074) elements - a reduction to at least 37.52% of the elements (on average 33.13%). In terms of run time the adaptive simulation used about 31.33% the computational time by yielding quantitatively the same result in terms of measured wave heights as well as currents.

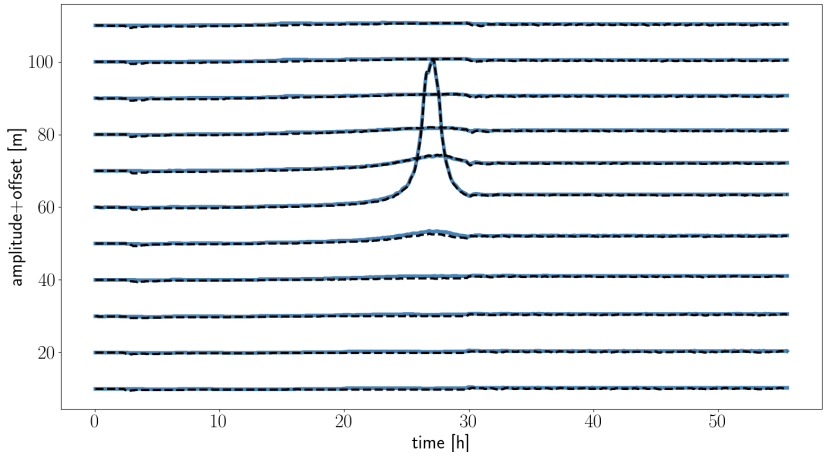

Figure 16: Idealised Hurricane Approaching a Linearly Sloping Beach: Waterfall plot of wave gauges G_k over time for uniform (black dashed line) and adaptive (blue solid line) simulation of Configuration 1. Values are plotted with an offset of $10k[m]$ for wave gauge G_k.

4 Conclusions and Future Work

In this study we have developed a Discontinuous Galerkin model on an unstructured, and dynamically adaptive triangular mesh that solves the fully 2D non-linear shallow water equations for the simulation of coastal flooding and idealised storm surges.

Numerical test cases demonstrate that the obtained model is inundation stable due to advanced slope limiting techniques [37] and maintains important conservation properties such as mass as well as integrated fluxes as described in section 3.1 for the simulation of a hypothetical embayment. Moreover, a steady state is achieved numerically in 3.2 in which a balance between pressure gradients and wind stress is simulated. In section 3.3, we show the robustness of the wind forcing and the effect of Coriolis forcing on wind-induced circulation. We furthermore see that the wind forcing is robust with respect to ramp up times hence no spurious artefacts are introduced.

Finally, in section 3.4, we show the capability of the model to simulate idealised hurricane storm surge using the wind parameterisation [16], hence making it suitable for simulation of realistic hurricanes such as 2008 Atlantic hurricane Ike or 2017 hurricane Ophelia. A sensitivity analysis furthermore reveals that the model is not sensitive to the choice of wind drag parameterisation or storm ramp up time. The observed variability of maximum wave heights (and therewith wave run up) with varying RMW confirms previously published studies, underlining the capability of the model to yield realistic results. Most notably, using dynamically adaptive unstructured meshes, we obtain virtually the same results at significantly less computational cost: The reduction was measured to be up to 70%. Overall this is to demonstrate that the developed model is suitable for the simulation of idealised hurricane storm surge and shows a satisfactory robustness and accuracy as well as adaptive mesh capabilities that help reduce computing costs significantly.

In this study, we have dealt with a number of idealised test cases and demonstrated the model's potential to use an unstructured mesh for the simulation of hurricane storm surge. The application of the presented model to more realistic data is beyond the scope of this paper and will be left for future research. The results presented, however, allow the conclusion that the presented method is suitable for application to hurricane storm surge modelling.

5 Acknowledgments

We kindly acknowledge funding by Science Foundation Ireland (SFI) under the research project "Understanding Extreme Nearshore Wave Events through Studies of Coastal Boulder Transport" (14/US/E3111) as well as by the Irish Research Council (IRC) under the research project "NIMBUS^3: Next-Generation Integrated Model for Better and Unified Storm Surge Simulations" (GOIPD/2018/248). Furthermore, we wish to acknowledge the DJEI/DES/SFI/HEA Irish Centre for High-End Computing (ICHEC) for the provision of computational facilities and support.

References

[1] Daniel S Abdi, Francis X Giraldo, Emil M Constantinescu, Lester E Carr, Lucas C Wilcox, and Timothy C Warburton. Acceleration of the IMplicit-EXplicit nonhydrostatic unified model of the atmosphere on manycore processors. *The International Journal of High Performance Computing Applications*, 33(2):242–267, 2019.

[2] D. C. Antonopoulos and V. A. Dougalis. Galerkin-finite element methods for the shallow water equations with characteristic boundary conditions. *IMA Journal of Numerical Analysis*, 37(1):266–295, 05 2016.

[3] Patrick L. Barnard, Li H. Erikson, Amy C. Foxgrover, Juliette A. Finzi Hart, Patrick Limber, Andrea C. ONeill, Maarten van Ormondt, Sean Vitousek, Nathan Wood, Maya K. Hayden, and Jeanne M. Jones. Dynamic flood modeling essential to assess the coastal impacts of climate change. *Scientific Reports*, 9(4309), 2019.

[4] S. Beckers, J. Behrens, and W. Wollner. Duality based error estimation in the presence of discontinuities. *Applied Numerical Mathematics*, 144:83 – 99, 2019.

[5] Jörn Behrens. *Adaptive Atmospheric Modeling*. Springer, 2006.

[6] Jörn Behrens and Michael Bader. Efficiency considerations in triangular adaptive mesh refinement. *Philosophical Transactions of the Royal Society A: Mathematical, Physical and Engineering Sciences*, 367(1907):4577 –4589, November 2009.

[7] Jörn Behrens, Natalja Rakowsky, Wolfgang Hiller, Dörthe Handorf, Matthias Läuter, Jürgen Päpke, and Klaus Dethloff. amatos: Parallel adaptive mesh generator for atmospheric and oceanic simulation. *Ocean Modelling*, 10(1-2):171–183, 2005.

[8] N. Beisiegel and F. Dias. Representation of Atlantic Hurricanes in MÉRA Data and Their Effect on Coastal Waves. In Emily Gleeson and Eoin Whelan, editors, *MÉRA Workshop Proceedings*. Met Éireann, 2019. submitted.

[9] Nicole Beisiegel. *High-order Adaptive Discontinuous Galerkin Inundation Modeling*. PhD thesis, Universität Hamburg, 2014.

[10] J. R. Davis and Y. P. Sheng. Development of a parallel storm surge model. *Int. J. Numer. Meth. Fluids*, 42:549 – 580, 2003.

[11] C. Dawson, E. J. Kubatko, J. J. Westerink, C. Trahan, C. Mirabito, C. Michoski, and N. Panda. Discontinuous Galerkin methods for modeling Hurricane storm surge. *Advances in Water Resources*, 34(9):1165–1176, 2011.

[12] P. Farrell, D. Ham, S. Funke, and M. Rognes. Automated Derivation of the Adjoint of High-Level Transient Finite Element Programs. *SIAM Journal on Scientific Computing*, 35(4):C369–C393, 2013.

[13] J. R. Garrat. Review of Drag Coefficients over Oceans and Continents. *Monthly Weather Review*, 105:915–929, 1977.

[14] Verena Hermann, Martin Käser, and Cristóbal E. Castro. Non-conforming hybrid meshes for efficient 2D wave propagation using the Discontinuous Galerkin method. *Geophys. J. Int.*, 184(2):746–758, 2011.

[15] Jan S. Hesthaven and Tim Warburton. *Nodal discontinuous Galerkin methods: algorithms, analysis, and applications*. Springer, 2008.

[16] Greg J. Holland. An Analytic Model of the Wind and Pressure Profiles in Hurricanes. *Mon. Weather Rev.*, 108:1212–1218, 1980.

[17] S. A. Hsu and Zhongde Yana. A Note on the Radius of Maximum Winds for Hurricanes. *Journal of Coastal Research*, 12(2):667–668, 1998. Coastal Education & Research Foundation, Inc.

[18] J. T. C. Ip, D. R. Lynch, and C. T. Friedrichs. Simulation of Estuarine Flooding and Dewatering with Application to Great Bay, New hampshire. *Estuarine, Coastal and Shelf Science*, 47:119–141, 1998.

[19] Jennifer L. Irish, Donald T. Resio, and Jay J. Ratcliff. The Influence of Storm Size on Hurricane Surge. *Journal of Physical Oceanography*, 38(9):2003–2013, 2008.

[20] Georges Kesserwani and Qiuhua Liang. Locally Limited and Fully Conserved RKDG2 Shallow Water Solutions with Wetting and Drying. *Journal of Scientific Computing*, 50(1):120–144, 2012.

[21] Michal A Kopera and Francis X Giraldo. Analysis of adaptive mesh refinement for IMEX discontinuous Galerkin solutions of the compressible Euler equations with application to atmospheric simulations. *Journal of Computational Physics*, 275:92–117, 2014.

[22] E.J. Kubatko, B.A. Yeager, and D.I.Ketcheson. Optimal Strong-Stability-Preserving Runge–Kutta Time Discretizations for Discontinuous Galerkin Methods. *Journal of Scientific Computing*, 60(2):313–344, 2014.

[23] W. G. Large and S. Pond. Open Ocean Momentum Flux Measurements in Moderate to Strong Winds. *Journal of Physical Oceanography*, 11(3):324–336, 1981.

[24] N. Lin, K. A. Emanuel, J. A. Smith, and E. Vanmarcke. Risk assessment of hurricane storm surge for New York City. *Journal of Geophysical Research: Atmospheres*, 115(D18), 2010.

[25] R.A. Luettich and J.J. Westerink. Implementation and Testing of Elemental Flooding and Drying in the ADCIRC Hydrodynamic Model. Technical report, DEPARTMENT OF THE ARMY, Coastal Engineering Research Center, Waterways Experiment Station, US Army Corps of Engineers, 1995. Final Contractors Report.

[26] K. T. Mandli and C. N. Dawson. Adaptive mesh refinement for storm surge. *Ocean Modelling*, 75:36–50, 2014.

[27] Kyle T. Mandli. *Finite Volume Methods for the Multilayer Shallow Water Equations with Applications to Storm Surges*. PhD thesis, University of Washington, July 2011.

[28] M. D. Piggott, G. J. Gorman, C. C. Pain, P. A. Allison, A. S. Candy, B. T. Martin, and M. R. Wells. A new computational framework for multi-scale ocean modelling based on adapting unstructured meshes. *International Journal for Numerical Methods in Fluids*, 56(8):1003–1015, 2008.

[29] M. D. Piggott, C. C. Pain, G. J. Gorman, D. P. Marshall, and P. D. Killworth. Unstructured adaptive meshes for ocean modeling. In H. Hasumi and M. W. Hecht, editors, *Ocean Modeling in an Eddying Regime*, pages 383–408. AGU, 2008.

[30] M. D. Powell. New findings on hurricane intensity, wind field extent, and surface drag coefficient behavior. Technical report, National Oceanic and Atmospheric Administration, 2007. Technical Report.

[31] J. Qiang, Q. Liang, G. Wang, and J. Zheng. Testing a Shock-Capturing Hydrodynamic Model for Storm Surge Simulation. *Proceedings of the Twenty-sixth (2016) International Ocean and Polar Engineering Conference Rhodes, Greece*, pages 747 –753, 2016.

[32] M. C. Rivara. Algorithms for Refining Triangular Grids Suitable for Adaptive and Multigrid Techniques. *International Journal for Numerical Methods in Engineering*, 20:745–756, 1984.

[33] R. Sanay and A. Valle-Levinson. Wind-Induced Circulation in Semienclosed Homogeneous, Rotating Basins. *Journal of Physical Oceanography*, 35:2520–2531, 2005.

[34] E. F. Toro. *Riemann solvers and numerical methods for fluid dynamics: a practical introduction*. Springer, 2009.

[35] Nelson Tull. Improving Accuracy of Real-Time Storm Surge Inundation Predictions. Master's thesis, North Carolina State University, Raleigh, North Carolina, 2018.

[36] S. Vater, N. Beisiegel, and J. Behrens. A limiter-based well-balanced discontinuous Galerkin method for shallow-water flows with wetting and drying: One-dimensional case. *Advances in Water Resources*, 85:1–13, 2015.

[37] S. Vater, N. Beisiegel, and J. Behrens. A limiter-based well-balanced discontinuous Galerkin method for shallow-water flows with wetting and drying: Triangular grids. *International Journal for Numerical Methods in Fluids*, 2019. in print.

[38] R. H. Weisberg and L. Zheng. Hurricane Storm Surge Simulations for Tampa Bay. *Estuaries and Coasts*, 29(6A):899–913, 2006.

[39] Zhiliang Xu, Xu-Yan Chen, and Yingjie Liu. A new rungekutta discontinuous galerkin method with conservation constraint to improve cfl condition for solving conservation laws. *Journal of Computational Physics*, 278:348 – 377, 2014.